

Performance of a nanoarchitected tin oxide@reduced graphene oxide composite as a shield against electromagnetic polluting radiation

Cite this: *RSC Adv.*, 2014, 4, 25904

Monika Mishra,^a Avanish Pratap Singh,^a Bhanu Pratap Singh^b and S. K. Dhawan^{*a}

Received 3rd March 2014
Accepted 20th May 2014
DOI: 10.1039/c4ra01860e
www.rsc.org/advances

Tin oxide nanoparticles architected with a reduced graphene oxide composite (SnO₂@RGO) have been synthesised by *in situ* reduction of graphene oxide in the presence of stannous chloride. The microwave shielding performance of SnO₂@RGO has been evaluated over the X-band (8.2–12.4 GHz) range. XRD and TEM studies show that the tin oxide nanoparticles are anchored uniformly onto the surface of the reduced graphene oxide sheets. A total electromagnetic interference shielding effectiveness in the order of 62 dB was achieved, which is more than the required values (~30 dB) desired for techno-commercial applications.

1. Introduction

Graphene and graphene-based composites with electro-conductive properties are very promising materials for numerous uses in technological applications, such as energy storage,¹ electro-optical devices,^{2,3} and electromagnetic shielding.^{4,5} With the rapid growth of the electronics industry, most communication devices have shifted towards a higher frequency range. For abundant electrical and electronic devices, electromagnetic interference (EMI) remains a technical task in terms of the proper matching of impedance. EMI tends to reduce the response in the performance of the equipment. The shielding of various electronic devices from mobile signals and EMI is important, and this is performed by microwave shielding materials.^{6,7} Most of the electromagnetic shields are ferrites,^{8–10} metallic magnetic materials,^{11–14} and carbon nanotube (CNT) composites.^{15–17} Usually, metals are used for this purpose, but the layers commonly stumbled upon in metal sheets tend to cause radiation seepages, which lessen the effectiveness of the shielding material. Graphene matrix composites that contain conductive fillers are most promising EMI-shielding materials.^{18,19} Impedance matching, defect polarization relaxation and electronic dipole relaxation are present in reduced graphene oxide, which help to improve electromagnetic shielding.²⁰ Thus, reduced graphene oxide shows improved microwave shielding when compared with graphite and carbon nanotubes and is likely to show better absorption than that compared to high quality graphene, making it a promising candidate as a microwave shielding material.^{21–23} Our previous

efforts based on graphene encourage us to search more and more for new types of composites of graphene.^{4,24–26} The present investigation is one of the most innovative efforts to discover new types of material for EMI shielding.

Recent advances in architecting graphene with different materials such as Fe₃O₄,²⁵ TiO₂ (ref. 27) and gold nanoparticles²⁸ inspire us to design SnO₂ decorated reduced graphene oxide (RGO) sheets. RGO–SnO₂ composites have attracted significant attention recently due to their potential applications.^{29,30} The combination of the high conductivity of the RGO sheets and tin oxide nanoparticles make it a constructive candidate for the next generation of microwave absorbing materials. Special attention is dedicated to reducing the reinforced particle size and allowing environmentally friendly synthesis conditions. Small, as low as 3–5 nm, average crystallite sizes have already been reported.^{31,32} Moreover, small size particles possess high anisotropy energy, which also contributes in the enhancement of their microwave shielding properties.

In this study, we attempt to architect RGO sheets using tin oxide nanoparticles *via* an *in situ* reduction of graphene oxide (GO) in the presence of stannous chloride and hydrochloric acid, for high-performance EMI shielding applications. The facile method used in this study has several advantages over traditional GO reduction methods such as an extra reducing agent *e.g.* hydrazine hydrate is not required for the reduction of GO to RGO and the *in situ* genesis of nanoparticles leads to uniform size particles on individual RGO sheets. Such architected SnO₂ decorated RGO sheets exhibit enhanced shielding effectiveness when compared to conventional EMI shielding materials. The resulting composite possesses high dielectric properties with moderate conductivity, making it a next-generation material for use in EMI shielding against electromagnetic pollution. The intended composite is promising and lightweight for a practical use of EMI shielding applications in the areas of stealth technology.

^aPolymetric & Soft Materials Section, CSIR-National Physical Laboratory, Dr K. S. Krishnan Road, New Delhi-110 012, India. E-mail: skdhawan@mail.nplindia.ernet.in; Fax: +91-11-25726938; Tel: +91-11-45609401

^bPhysics and Engineering of Carbon, CSIR-National Physical Laboratory, Dr K. S. Krishnan Road, New Delhi-110 012, India

2. Experimental section

2.1 Materials

Natural graphite powder (purity 99.5%, particle size 50 μm) procured from Loba Chemie, India, has been used to synthesize GO. Stannous(II) chloride dihydrate ($\text{SnCl}_2 \cdot 2\text{H}_2\text{O}$) and NaNO_3 were obtained from Qualigens Fine Chemicals, India; HCl from Rankem, India; ammonia and KMnO_4 from Fisher scientific, India; and H_2SO_4 and ethanol were obtained from Merck, India. Double distilled water with a specific resistivity of $10^6 \Omega \text{ cm}$ was used for preparing aqueous solutions and for filtration purposes.

2.2 Preparation of materials

Synthesis of tin oxide. $\text{SnCl}_2 \cdot 2\text{H}_2\text{O}$ (112.81 g) was dissolved in HCl (37 wt%, 10 mL) and diluted with distilled water (500 mL) to give a SnCl_2 -HCl solution. In order to form a uniform solution and maintain the pH at approximately 10, a certain amount of ammonia (25%) was added at a controlled rate (0.01 – 0.1 mL min^{-1}) to the SnCl_2 -HCl solution with vigorous stirring. The resulting solution was then stirred at 90°C for 6 h. The precipitate obtained was separated by centrifugation and washed with distilled water to remove the excess chloride ions.

The resulting product was dried in a vacuum oven at 110°C for 24 h followed by calcination (at 400°C for 5 h under an N_2 atmosphere) to improve of crystallinity of the SnO_2 .³¹

Synthesis of SnO_2 decorated RGO sheets. The chemical reduction of graphene oxide (GO) was carried out in the presence of SnCl_2 to fabricate SnO_2 decorated RGO. Prior to this, GO has been synthesised. The detailed method of GO synthesis was discussed in our earlier report.²⁴ In brief, commercially available graphite powder (5 g) and NaNO_3 (5 g) was mixed into concentrated H_2SO_4 (230 mL). KMnO_4 (40 g) was gradually added with stirring and cooling, so that the temperature of the mixture did not reach beyond 20°C . The mixture was then stirred at 35°C for 2 h, and deionized water (200 mL) added. The reaction was stirred for 1 h followed by the addition of a large amount of deionized water (300 mL) and 30% H_2O_2 solution (30 mL), causing violent effervescence and an increase in temperature to 100°C , after which the color of the suspension changes to bright yellow. The suspension was washed with a solution of HCl in order to remove the metal ions. The paste collected was dried at 60°C . 2 g of the GO powder was dispersed in 500 mL of distilled water followed by stirring and ultrasonication for 1 h to prepare the solution of GO.

A typical preparation process for SnO_2 decorated RGO is as follows: 14 g of $\text{SnCl}_2 \cdot 2\text{H}_2\text{O}$ was added to 500 mL HCl solution

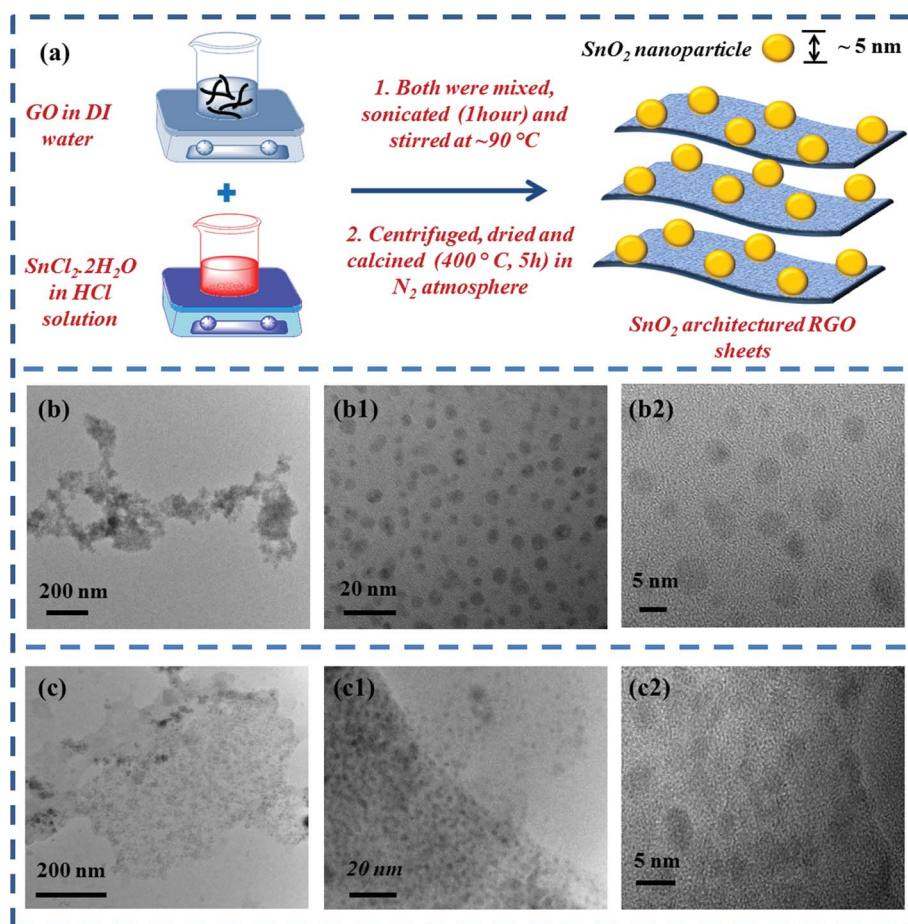


Fig. 1 (a) A schematic representation of the architected SnO_2 nanoparticles on the surface of the RGO sheets, (b) TEM images of the SnO_2 nanoparticles at different magnifications and (c) TEM images of the as-synthesized SnO_2 @RGO composite.

(100 mL L⁻¹ of 37 wt% HCl). Then, this solution was mixed with the GO solution and sonicated for 1 h. The resulting mixture was stirred at 90 °C for 6 h. SnO₂@RGO was collected after several washings with water through centrifugation, then dried in a vacuum oven at 100 °C. Calcination (400 °C for 5 h under a N₂ atmosphere) was carried out to improve the crystallinity of SnO₂.³¹ The possible reaction mechanism can be written as follows:



A schematic representation of RGO decoration using SnO₂ nanoparticles is shown in Fig. 1a.

2.3 Materials characterization

The morphology of the RGO–SnO₂ composites was characterized by transmission electron microscopy (TECNAI G²T30, u–TWIN) at an acceleration voltage of 300.0 kV. X-ray diffraction (XRD) measurements were performed on a D8 Advance XRD (Bruker) using CuK α radiation ($\lambda = 1.54 \text{ \AA}$) in the scattering range (2θ) of 10°–80° with a scan rate of 0.02° s⁻¹ and slit width of 0.1 mm. FT-IR spectra were recorded on a Nicolet 5700 spectrometer in transmission mode in the wave number range of 400–4000 cm⁻¹. Spectroscopic grade KBr pellets were used for collecting the spectra with a resolution of 4 cm⁻¹ performing 32 scans. Raman analysis was carried out using a Renishaw inVia Reflex spectrometer, UK with an excitation source of 514.5 nm. The resolution of the instrument was less than 1.0 cm⁻¹. The dc electrical conductivity has been measured using a standard four-probe technique, in order to eliminate contact resistance effects, using a Keithley programmable current source (model 6221) and nano voltmeter (model 2182A). Electromagnetic shielding and dielectric measurements have been carried out using an Agilent E8362B Vector Network Analyzer in the 8.2–12.4 GHz (X-band) microwave range. The composite has compacted in a piston cylinder assembly at 60 MPa for 5 min into different thickness rectangle pellets with a dimension to fit the waveguide dimensions.

3. Results and discussion

3.1 Morphological analysis

Fig. 1b and c demonstrate the transmission electron microscopy (TEM) images of the SnO₂ nanoparticles and SnO₂ decorated RGO. Fig. 1b shows the SnO₂ nanoparticles at different magnifications. Higher magnification images (Fig. 1b1 and 1b2) confirm that all particles are of 3–5 nm diameter. It is evident that the RGO sheet was uniformly decorated by a large quantity of SnO₂ nanoparticles, and the outline of both RGO and SnO₂ nanoparticles can be clearly seen as depicted in Fig. 1c. Higher magnification images (Fig. 1c2 and 1c3) revealed that the SnO₂ nanoparticles have grown on the surface of the RGO sheet and were distributed over the RGO's surface. SnO₂ nanoparticles can exist densely on both sides of these sheets. Most importantly, there are no vacant areas on the RGO sheets that are not decorated with SnO₂ nanoparticles. It is worthy to notice that these SnO₂ nanoparticles are strongly attached to the RGO sheets, because sonication was applied during the preparation

of the TEM samples, indicating excellent bonding between the RGO and SnO₂ nanoparticles. The presence of dielectric nanoparticles on a conducting surface is helpful for enhancing the shielding properties of the material.

3.2 Structural analysis

The crystal structure of GO, RGO and RGO–SnO₂ was characterized by XRD and the results displayed in Fig. 2a. The powder X-ray diffraction pattern of GO shows a diffraction peak around 10.2°, which corresponds to the (002) reflection of the stacked GO sheets. It shows an interlayer spacing of 0.86 nm for GO, which is more than graphite with an interlayer spacing of 0.34 nm. It is due to the introduction of oxygen containing groups on the GO sheets. Chemical reduction of GO to RGO leads to broadening and shifting of the XRD peak to around 24.9° corresponding to an interlayer spacing of about 0.36 nm. This indicates the presence of residual oxygenated groups on the RGO sheets. For SnO₂@RGO, there are no diffraction peaks

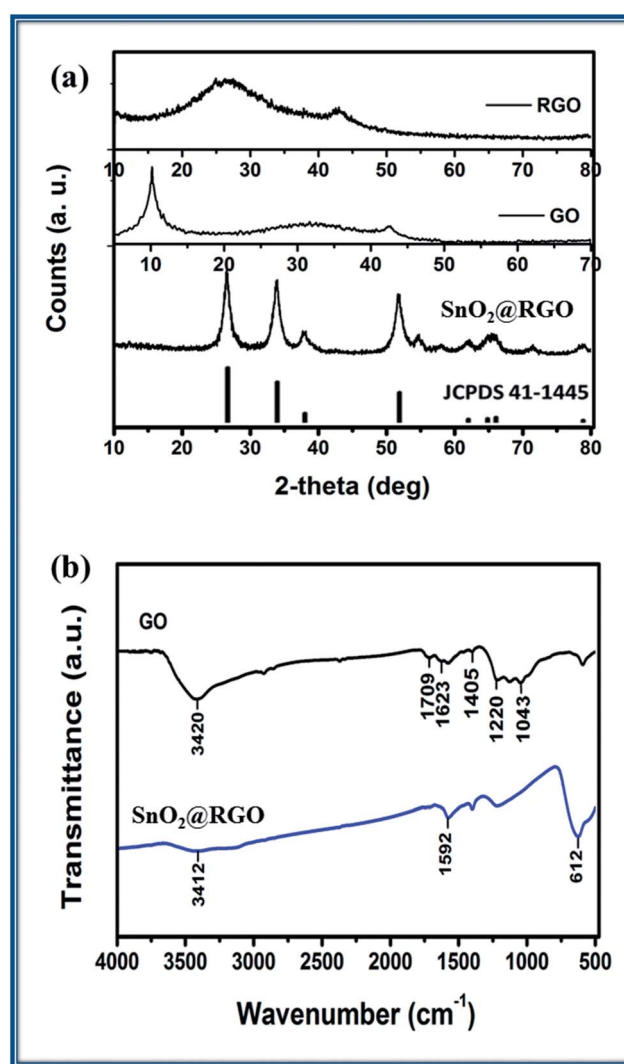


Fig. 2 (a) X-ray diffraction patterns of SnO₂@RGO, GO and RGO (b) comparison of the FT-IR spectra of the GO and SnO₂@RGO composite.

corresponding to GO, indicating the reduction of GO to RGO by stannous ions. The diffraction patterns and relative intensities of the synthesized SnO₂ matched well with standard SnO₂ (JCPDS 41-1445), demonstrating that the nanoparticles were SnO₂ and shows that the diffraction peaks of crystalline SnO₂ nanoparticles are clearly distinguishable. It could be indexed to the tetragonal SnO₂ phase (JCPDS 41-1445). The XRD peaks of the composite appearing at about $2\theta = 26.5, 33.9,$ and 51.6 can be indexed to the diffraction planes of SnO₂ (110), (101), and (211), respectively. The mean particle size (D) of the SnO₂ nanoparticles was calculated by applying the Scherrer equation to the (110) plane diffraction peak and found to be 3–5 nm in the SnO₂@RGO composite.

3.3 FT-IR spectroscopy

Fig. 2b shows the FT-IR spectra of GO and SnO₂@RGO. The FT-IR spectra of GO confirmed the presence of oxygen-containing groups, such as C–OH at 3420 cm^{-1} , C–O–C at 1220 cm^{-1} , and C=O in the carboxylic acid moieties at 1709 cm^{-1} . Other characteristic vibrations were the O–H deformation peak at 1405 cm^{-1} and the C–O stretching peak at 1043 cm^{-1} . The peak at 1623 cm^{-1} was assigned to the contributions from the skeletal vibrations of the graphitic domains. For SnO₂@RGO, the carboxylic acid vibration band at 1709 cm^{-1} disappeared. A weak signal for the C–OH stretching vibration at 3412 cm^{-1} could be ascribed to the vibrations of the adsorbed water molecules which is assigned to the Eu mode of SnO₂ (anti-symmetric O–Sn–O stretching). The presence of the Eu mode (a band located at 612 cm^{-1}) in SnO₂@RGO indicates the incorporation of SnO₂ particles on the RGO sheets. Additionally, the spectrum of the SnO₂@RGO composite shows an absorption band at 1592 cm^{-1} (C=C stretching), indicating the restoration of the graphene network on reduction. Therefore, it could be concluded that GO was reduced by the stannous ions.

3.4 Raman spectroscopy

Raman spectroscopy is a very powerful tool for investigating the interactions or bonding between two components.³³ To elucidate the graphitic structure of GO, RGO and the interactions among RGO, and SnO₂ nanoparticles, Raman spectroscopy was conducted in a spectral range of $100\text{--}3300\text{ cm}^{-1}$. Fig. 3 shows the Raman spectra of GO, RGO, and SnO₂@RGO composite. The Raman spectra of GO and RGO consist of three prominent characteristic peaks, namely the D band (disorder-induced band), the G band (the tangential mode of graphitic structure), and the G' (or 2D) band. The G and D bands are due to the doubly degenerate zone centre E_{2g} mode ($\sim 1580\text{--}1600\text{ cm}^{-1}$) and the breathing modes of six atom rings which appears at $\sim 1350\text{ cm}^{-1}$ due to the presence of defects in the graphite, respectively.³⁴ In the Raman spectrum of RGO, the D, G and 2D peak position values confirm the formation of RGO. Raman spectrum of pure SnO₂ nanoparticles reveals all the characteristic bands of SnO₂ in the low frequency region, *i.e.*, $436, 479$ (E_g), 564 (S₁), 633 (A_{1g}).³⁵ All these peaks are suppressed in the SnO₂@RGO composite because of the highly intense graphitic peaks present in the RGO sheets. Furthermore, the interactions

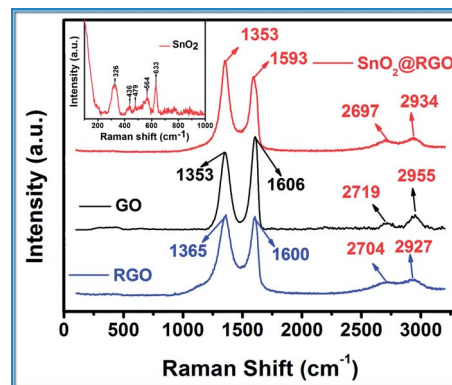


Fig. 3 Raman spectra of RGO, GO, and SnO₂ decorated RGO sheets. Inset image shows the Raman spectrum of the SnO₂ nanoparticles.

between the RGO and SnO₂ nanoparticles are clearly seen by the red shift in peaks of RGO from 1365 to 1353 cm^{-1} in the D band and from 1600 to 1593 cm^{-1} in the G band. Slight shifting in the bands is an evidence of interaction between these components. Additionally, a slight shift was also observed in the G' band. The I_D/I_G value of SnO₂@RGO is higher (1.22) than RGO (1.02). It also suggests the interaction of SnO₂ into the RGO sheet because at the time of the synthesis of the SnO₂@RGO, SnO₂ interacts on the available defect sites of the RGO sheet or on further occurrence of defect sites at the time of architecturing the SnO₂ nanoparticles onto the RGO surface.

3.5 Shielding effectiveness measurement

EMI SE of any material is the sum of the contributions from the absorption (SE_A), reflection (SE_R) and multiple reflections (SE_M) of the EM energy:^{36–38}

$$SE = -10 \log(P_T/P_I) = SE_R + SE_A + SE_M \quad (1)$$

where: P_I and P_T are the power of incident and transmitted EM waves, respectively.

According to Schelkunoff's theory, SE_M can be ignored in all practical applications where the shield is thicker than the skin depth (δ). For a material, the skin depth (δ) is the distance up to which the intensity of the EM wave decreases to $1/e$ of its original strength. δ is related to angular frequency, relative permeability and total conductivity:

$$\sigma_T = (\sigma_{dc} + \sigma_{ac}) \quad (2)$$

Fig. 4a–d shows the variation of the SE with frequency in the 8.2–12.4 GHz range. From Fig. 4a, the values of SE for the SnO₂@RGO composite (45.8 dB) is significantly higher than that of both RGO (32.5 dB) and SnO₂ (14.2 dB) at a critical thickness of 3 mm. It proposed that the addition of a dielectric filler enhances the SE of RGO. Therefore, SnO₂@RGO is a better option compared to the SnO₂ and RGO composites independently. We also explored the effect of varying the thickness of the composites on the EMI shielding performance. For this, rectangular pallets of different thicknesses (1.0 mm, 2.0 mm,

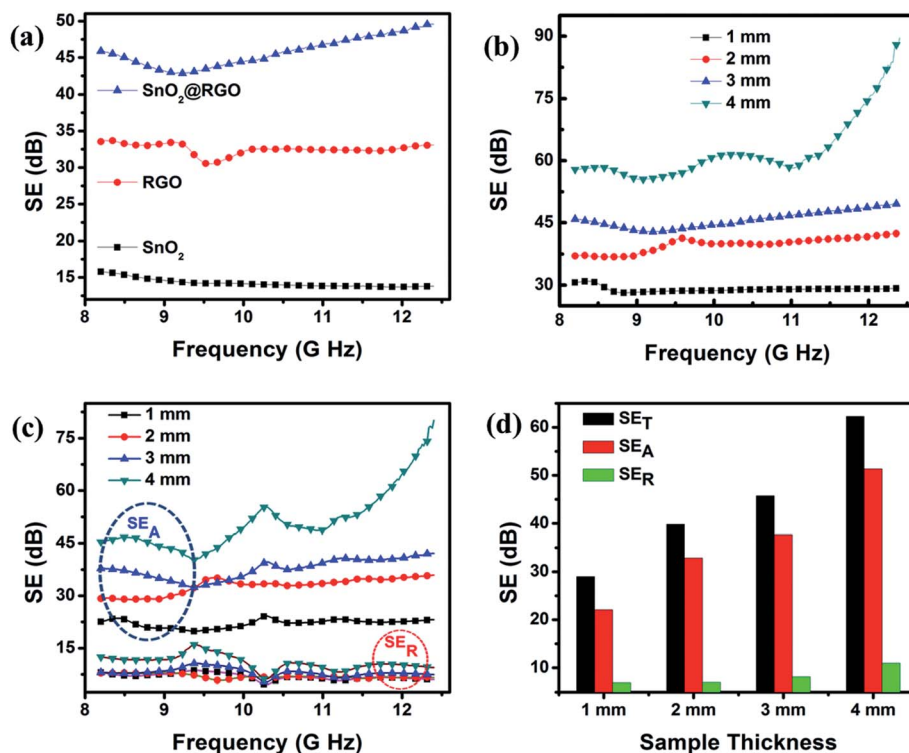


Fig. 4 (a) Variation in EMI shielding effectiveness SE_T of SnO_2 , RGO and the $SnO_2@RGO$ composite at a critical thickness of 3 mm, (b) behavior of SE_T for the $SnO_2@RGO$ composite at different thicknesses (c) behavior of SE_A and SE_R with frequency for different thicknesses of the $SnO_2@RGO$ composite and (d) SE_T , SE_A and SE_R for different thicknesses of the $SnO_2@RGO$ composite.

3.0 mm and 4.0 mm, respectively) were placed in the X-band sample holder and SE measured in the frequency range of 8.2–12.4 GHz. The plot of microwave SE versus frequency for $SnO_2@RGO$ having four different thicknesses are shown in Fig. 4b. The value of SE_T is 29 dB for the sample with a thickness of 1 mm and reached to 62 dB for the 4.0 mm thick sample.

The terms SE_R and SE_A can be defined as:^{25,38}

$$SE_R = -10 \log(1 - R) \quad (3)$$

$$SE_A = -10 \log(1 - A_{\text{eff}}) = -10 \log(T/1 - R). \quad (4)$$

Therefore, the effective absorbance (A_{eff}) can be described with respect to the power of the effectively incident EM wave inside the shielding material.

$$A_{\text{eff}} = (1 - R - T)/(1 - R) \quad (5)$$

In terms of dielectric losses the SE_A can also be written as:²⁵

$$SE_A (\text{dB}) = 20d \sqrt{\frac{\mu\omega^2 \epsilon_o \epsilon''}{2}} \log e \quad (6)$$

In terms of tan delta the above equation can be written as:

$$SE_A (\text{dB}) = 20d \sqrt{\frac{\mu\omega^2 \epsilon_o \epsilon' \tan \delta}{2}} \log e \quad (7)$$

i.e. SE_A is directly proportional to tan delta.

The calculated SE_A and SE_R obtained from the experimental scattering parameters (S_{11} , S_{22} , S_{12} , S_{21}) are plotted in Fig. 4c. The values of SE_A for the $SnO_2@RGO$ composite considerably increase with an increase in thickness over the entire frequency range. The SE_A values of the composite with 1, 2, 3 and 4 mm thickness are in the range of 22.58–23.15, 29.19–35.90, 37.80–42.09 and 45.39–80.14, respectively. In contrast, the values of SE_R are very low when compared to SE_A . Moreover, the change in SE_R is very small with an increasing thickness. Therefore, for the $SnO_2@RGO$ composite, the mechanism of shielding is mainly the absorption of EM waves due to the highly conductive composite and the absorption is proportional to the thickness of the composite material. Fig. 4d shows the overall changes in % attenuation with thickness in which changes in reflection loss with increasing thickness is very small compared to the absorption. According to the shielding theory, SE_A becomes more dominant when compared to SE_R in the microwave range. This may be caused by the shallow skin depth and high conductivity (σ_{ac}) values at such high frequencies.^{39,40} Although the electrical conductivity of $SnO_2@RGO$ is high (13.74 S cm^{-1}), it is much smaller than that of graphene reported theoretically. This is because the inter transport of charge carriers in $SnO_2@RGO$ is a complex phenomenon of electron tunneling and hopping, and is different from the single layer of graphene.^{5,25,38,41–43} Furthermore, the conductivity of the $SnO_2@RGO$ composite is acceptable because the insulating SnO_2 particles hinder the free flow of electrons in the $SnO_2@RGO$ composite.

The observed high shielding effectiveness could be explained in terms of dielectric loss. According to the EM theory, dielectric losses are the result of complex phenomena like natural resonance, dipole relaxation, electronic polarization and its relaxation, and certainly the unique structure of the shield. When the frequency of the applied field is increased, the electrons present in the system cannot reorient themselves fast enough to respond to the applied electric field and improves the dielectric constant. The SnO₂ nanoparticles anchored on the top surface of the RGO sheets act as a polarized center and improves polarization, which results in more microwave shielding. High electrical conductivity of SnO₂@RGO also enhances the shielding properties. SnO₂ nanoparticles act as tiny dipoles, which get polarized in the presence of an EM field and result in better microwave shielding.

The curves in Fig. 4c exhibit broad multi peaks, which imply the presence of natural resonance caused by the enhanced surface anisotropy of the small size of SnO₂ particles. Anisotropy energy of the small sized-materials,⁴⁴ especially in the nanoscale, would be higher due to surface anisotropic field due to the small size effect.⁴⁵ The higher anisotropy energy also contributes in the enhancement of the microwave shielding. Interfacial polarization occurs in heterogeneous media due to accumulation of charges at the interfaces and the formation of dipoles. Interfaces among tin oxide nanoparticles and RGO sheets further contribute to dielectric losses.

From these results, we conclude that the filling of SnO₂ nanoparticles exhibit better microwave shielding properties in comparison with pristine SnO₂ nanoparticles, pure RGO, γ -Fe₂O₃ nanoparticles, RGO-iron oxide composite, and MnO₂ decorated graphene nanoribbons reported earlier.^{46,47}

Dielectric permittivities were also investigated in order to understand the microwave shielding properties and dielectric loss mechanism of the SnO₂@RGO composite in detail. Fig. 5 shows the permittivity (ϵ'), permittivity loss (ϵ'') and tangent loss ($\tan \delta = \epsilon''/\epsilon'$) as a function of frequency for the SnO₂@RGO composite at a thickness of 3 mm. The permittivity symbolizes the intensity of polarization or the electrical energy storage ability of a material. The permittivity loss represents the energy loss during the activation by an EM wave. The highest value of ϵ'

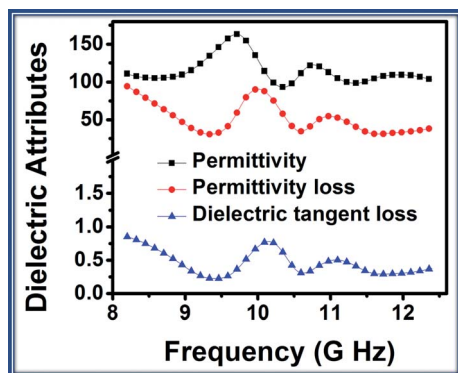


Fig. 5 Frequency dependence of the permittivity, permittivity loss and dielectric tangent loss of the SnO₂@RGO composite.

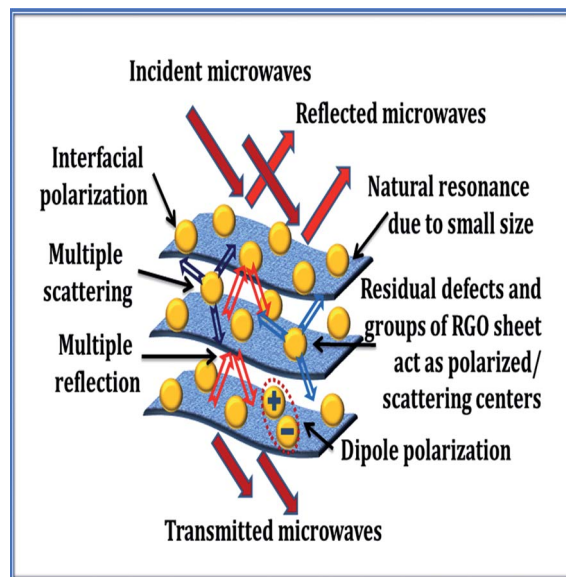


Fig. 6 A schematic presentation of the possible microwave shielding mechanisms in the SnO₂@RGO composite.

was 160 observed at 9.6 GHz. The value of ϵ'' is lower than ϵ' , and it fluctuates from 94 to 32 at 8.2 to 12.4 GHz. The values of the dielectric tangent loss were observed in the range of 0.85 to 0.36. The high value of ϵ'' and $\tan \delta$ for the SnO₂@RGO composite exhibit high dielectric losses. Interestingly, there are two humps observed in the dielectric tangent loss, which proposed that the two main phenomenas are responsible for dielectric losses. These may be interfacial polarization between the SnO₂ nanoparticles and RGO sheets and the effective anisotropy energy of the SnO₂@RGO composite. In the effective anisotropy energy, the parallel (RGO sheets are in a plane) and random alignment of the RGO sheets were of particular importance. According to the physics principles, the polarization intensity is directly proportional to the displacement of positive and negative charges during the activation by an EM wave. When the EM waves incident perpendicular to the RGO plane, the effective anisotropy energy is higher as the polarization intensity is higher in the plane direction. Therefore, contribution to the total EMI SE is higher when the EM wave incident is perpendicular to the RGO plane than that compared to when the EM wave incident is parallel to the RGO plane.⁵ Furthermore, the existence of residual defects/groups in the RGO sheet⁴⁸ and multiple reflections within the shield enhances the microwave shielding ability of the composites. Further, to give a visual demonstration of the microwave shielding mechanism as discussed above a schematic is given in Fig. 6. The results for the SnO₂@RGO composite illustrates that such structures could be potentially used as microwave shielding materials.

4. Conclusions

In summary, we have successfully designed high performance tin oxide nanoparticles decorated RGO for suppressing electromagnetic pollution. The presence of the dielectric filler SnO₂

nanoparticles on the RGO sheets enhances the dielectric losses, which can be attributed to natural resonance, dipole relaxation, electronic polarization-related relaxation, interfacial polarization and the effective anisotropy energy. Moreover, this unique SnO₂@RGO composite contributes to more scattering and leads to the high shielding effectiveness (SE_T ~ 62 dB at a thickness of 4 mm) when compared to conventional materials. This ingenious lightweight nanocomposite with outstanding shielding properties pushes its promising applications as a next generation building block material for EMI shielding and stealth technology.

Acknowledgements

The author Monika Mishra expresses her thanks to Prof. R. C. Budhani, Director, NPL, for his keen interest in the work. The authors express their thanks to the Ministry of New and Renewable energy for sponsoring the project. The authors thank Mr Dinesh Singh for recording the TEM images of the samples. We also thank Dr R. P. Pant for XRD measurements.

References

- Z.-S. Wu, G. Zhou, L.-C. Yin, W. Ren, F. Li and H.-M. Cheng, *Nano Energy*, 2012, **1**, 107–131.
- X. Wang, L. Zhi and K. Mullen, *Nano Lett.*, 2007, **8**, 323–327.
- M. Liu, X. Yin, E. Ulin-Avila, B. Geng, T. Zentgraf, L. Ju, F. Wang and X. Zhang, *Nature*, 2011, **474**, 64–67.
- A. P. Singh, M. Mishra, P. Sambyal, B. K. Gupta, B. P. Singh, A. Chandra and S. K. Dhawan, *J. Mater. Chem. A*, 2014, **2**, 3581–3593.
- N. Yousefi, X. Sun, X. Lin, X. Shen, J. Jia, B. Zhang, B. Tang, M. Chan and J.-K. Kim, *Adv. Mater.*, 2014, DOI: 10.1002/adma.201305293.
- T. Xia, C. Zhang, N. A. Oyler and X. Chen, *Adv. Mater.*, 2013, **25**, 6905–6910.
- X. C. Tong, *Advanced Materials and Design for Electromagnetic Interference Shielding*, Taylor & Francis, 2008.
- E. A. Maguire and D. W. Readey, *J. Am. Ceram. Soc.*, 1976, **59**, 434–437.
- W. Li, X. Qiao, H. Zhao, S. Wang and Q. Ren, *J. Nanosci. Nanotechnol.*, 2013, **13**, 793–798.
- K. Khan, *J. Supercond. Novel Magn.*, 2014, **27**, 453–461.
- W. Xie, H. Cheng, Z. Chu, Y. Zhou, G. Tang and Y. Xu, *J. Wuhan Univ. Technol., Mater. Sci. Ed.*, 2007, **22**, 218–220.
- M. Matsumoto and Y. Miyata, *IEEE Trans. Magn.*, 1997, **33**, 4459–4464.
- V. M. Petrov and V. V. Gagulin, *Inorg. Mater.*, 2001, **37**, 93–98.
- E. J. Borchers, C. E. Boyer, C. D. Hoyle and R. J. Kuo, Google Patents, US5085931 A, 1992.
- A. P. Singh, B. K. Gupta, M. Mishra, Govind, A. Chandra, R. B. Mathur and S. K. Dhawan, *Carbon*, 2013, **56**, 86–96.
- A. Saib, L. Bednarz, R. Daussin, C. Bailly, L. Xudong, J. Thomassin, C. Pagnouille, C. Detrembleur, R. Jerome and I. Huynen, *IEEE Trans. Microwave Theory Tech.*, 2006, **54**, 2745–2754.
- J.-M. Thomassin, X. Lou, C. Pagnouille, A. Saib, L. Bednarz, I. Huynen, R. Jérôme and C. Detrembleur, *J. Phys. Chem. C*, 2007, **111**, 11186–11192.
- H.-B. Zhang, Q. Yan, W.-G. Zheng, Z. He and Z.-Z. Yu, *ACS Appl. Mater. Interfaces*, 2011, **3**, 918–924.
- X. Bai, Y. Zhai and Y. Zhang, *J. Phys. Chem. C*, 2011, **115**, 11673–11677.
- C. Wang, X. Han, P. Xu, X. Zhang, Y. Du, S. Hu, J. Wang and X. Wang, *Appl. Phys. Lett.*, 2011, **98**, 072906.
- W. Choi and J. Lee, *Graphene: Synthesis and Applications*, Taylor & Francis, 2011.
- H. Seul Ki, K. Ki Yeong, K. Taek Yong, K. Jong Hoon, P. Seong Wook, K. Joung Ho and C. Byung Jin, *Nanotechnology*, 2012, **23**, 455704.
- R. Murali, *Graphene Nanoelectronics: From Materials to Circuits*, Springer, 2011.
- M. Mishra, A. P. Singh and S. K. Dhawan, *J. Alloys Compd.*, 2013, **557**, 244–251.
- A. P. Singh, P. Garg, F. Alam, K. Singh, R. B. Mathur, R. P. Tandon, A. Chandra and S. K. Dhawan, *Carbon*, 2012, **50**, 3868–3875.
- P. Sambyal, A. P. Singh, M. Verma, M. Farukh, B. P. Singh and S. K. Dhawan, *RSC Adv.*, 2014, **4**, 12614–12624.
- X.-Y. Zhang, H.-P. Li, X.-L. Cui and Y. Lin, *J. Mater. Chem.*, 2010, **20**, 2801–2806.
- Z. Xiong, L. L. Zhang, J. Ma and X. S. Zhao, *Chem. Commun.*, 2010, **46**, 6099–6101.
- S. Humaira, K. C. Kemp, C. Vimlesh and S. K. Kwang, *Nanotechnology*, 2012, **23**, 355705.
- X. Zhu, Y. Zhu, S. Murali, M. D. Stoller and R. S. Ruoff, *J. Power Sources*, 2011, **196**, 6473–6477.
- J. Zhang, Z. Xiong and X. S. Zhao, *J. Mater. Chem.*, 2011, **21**, 3634–3640.
- S. Sladkevich, J. Gun, P. V. Prikhodchenko, V. Gutkin, A. A. Mikhaylov, V. M. Novotortsev, J. X. Zhu, D. Yang, H. H. Hng, Y. Y. Tay, Z. Tsakadze and O. Lev, *Nanotechnology*, 2012, **23**, 485601.
- T. K. Gupta, B. P. Singh, S. R. Dhakate, V. N. Singh and R. B. Mathur, *J. Mater. Chem. A*, 2013, **1**, 9138–9149.
- A. C. Ferrari, J. C. Meyer, V. Scardaci, C. Casiraghi, M. Lazzeri, F. Mauri, S. Piscanec, D. Jiang, K. S. Novoselov, S. Roth and A. K. Geim, *Phys. Rev. Lett.*, 2006, **97**, 187401.
- A. Diéguez, A. Romano-Rodríguez, A. Vilà and J. R. Morante, *J. Appl. Phys.*, 2001, **90**, 1550–1557.
- A. M. Nicolson and G. F. Ross, *IEEE Trans. Instrum. Meas.*, 1970, **19**, 377–382.
- W. B. Weir, *Proc. IEEE*, 1974, **62**, 33–36.
- B. Wen, X. X. Wang, W. Q. Cao, H. L. Shi, M. M. Lu, G. Wang, H. B. Jin, W. Z. Wang, J. Yuan and M. S. Cao, *Nanoscale*, 2014, **6**, 5754–5761.
- N. C. Das, D. Das, T. K. Khastgir and A. C. Chakraborty, *Composites, Part A*, 2000, **31**, 1069–1081.
- N. F. Colaneri and L. W. Shacklette, *IEEE Trans. Instrum. Meas.*, 1992, **41**, 29.
- C. Gómez-Navarro, R. T. Weitz, A. M. Bittner, M. Scolari, A. Mews, M. Burghard and K. Kern, *Nano Lett.*, 2007, **7**, 3499–3503.

- 42 S. R. Pathipati, E. Pavlica, E. Treossi, R. Rizzoli, G. P. Veronese, V. Palermo, L. Chen, D. Beljonne, J. Cai and R. Fasel, *Org. Electron.*, 2013, **14**, 1787–1792.
- 43 P. Lian, X. Zhu, S. Liang, Z. Li, W. Yang and H. Wang, *Electrochim. Acta*, 2011, **56**, 4532–4539.
- 44 D. L. Leslie-Pelecky and R. D. Rieke, *Chem. Mater.*, 1996, **8**, 1770–1783.
- 45 Y.-J. Chen, P. Gao, R.-X. Wang, C.-L. Zhu, L.-J. Wang, M.-S. Cao and H.-B. Jin, *J. Phys. Chem. C*, 2009, **113**, 10061–10064.
- 46 K. Singh, A. Ohlan, V. H. Pham, B. R. S. Varshney, J. Jang, S. H. Hur, W. M. Choi, M. Kumar, S. K. Dhawan, B.-S. Kong and J. S. Chung, *Nanoscale*, 2013, **5**, 2411–2420.
- 47 T. K. Gupta, B. P. Singh, V. N. Singh, S. Teotia, A. P. Singh, I. Elizabeth, S. R. Dhakate, S. K. Dhawan and R. B. Mathur, *J. Mater. Chem. A*, 2013, **2**, 4256–4263.
- 48 X. Sun, J. He, G. Li, J. Tang, T. Wang, Y. Guo and H. Xue, *J. Mater. Chem. C*, 2013, **1**, 765–777.